Journal of Crystal Growth 465 (2017) 27–33

Contents lists available at ScienceDirect

Journal of Crystal Growth

journal homepage: www.elsevier.com/locate/crys

Facile synthesis and structure characterization of hexagonal tungsten bronzes crystals

Jiann-Shing Lee *, Hao-Chuan Liu, Gao-De Peng, Yawteng Tseng

Department of Applied physics, National Pingtung University, Taiwan, ROC

ARTICLE INFO

Article history:
Received 5 November 2016
Received in revised form 14 February 2017
Accepted 26 February 2017
Available online 28 February 2017
Communicated by T.F. Kuech

Keywords:
A1. Crystal structure
A1. X-ray diffraction
A2. Single crystal growth
B1. Tungsten bronze

ABSTRACT

A facile molten-salt route was used to synthesize hexagonal $Cs_{0.33}WO_3$, $Rb_{0.33}WO_3$ and $K_{0.30}WO_3$ crystals. The three isostructural compounds were successfully prepared from the reaction of M*x*WO_3 powders (M = Cs, Rb, K) in the CsCl/NaCl, RbCl/NaCl and KCl/NaCl fluxes, respectively. The structure determination and refinement, based on single-crystal X-ray diffraction data, are in agreement with previous works, possessing space group $P6_3/mcm$. The *a* and *c* parameters vary non-linearly with increasing radii of the M^+ cations (r_M) that is coordinated to twelve oxygen atoms. Both the volumes of unit-cell and WO_6 octahedra vary linearly with r_M, which become smaller from $Cs_{0.33}WO_3$ to $K_{0.30}WO_3$. The distortion of WO_6 octahedra as well as isotropic displacement parameters increases from $Cs_{0.33}WO_3$ to $K_{0.30}WO_3$. The geometry of the WO_6 octahedron becomes more regular with increasing r_M. These structural trends arise from the effective size of the M^+ cation.

© 2017 Elsevier B.V. All rights reserved.

1. Introduction

The oxygen deficiency in tungsten oxides results in a complex-ordered structure known as the Magneli structure, while the ternary addition of the cation leads to the tungsten bronze structure. The tungsten bronzes (M*x*WO_3) are typical example of non-stoichiometric compounds, in which M is a univalent metal and *x* lies between 0 and 1 [1,2]. They crystallize in a number of different phases and represent an unusually interesting series with properties ranging from metallic to semiconducting depending on the univalent metal M [3]. There are four structurally different tungsten bronze phases namely, perovskite tungsten bronze (PTB), hexagonal tungsten bronze (HTB), tetragonal tungsten bronze (TTB) and intergrowth tungsten bronze (ITB) [3,4]. The crystal structure of sodium tungsten bronzes is of PTB and HTB. Tetragonal Na*x*WO_3 for $x = 0.25$ as well as 0.35 are identified, and cubic Na*x*WO_3 for *x* values from 0.45 to 0.85 [5]. The Na*x*WO_3 film crystallized with the hexagonal symmetry of space group P6/mmm have also been reported [6]. Another three alkali-HTB compounds, Cs*x*WO_3, Rb*x*WO_3 and K*x*WO_3 have been found with a space group of $P6_3/mcm$ or $P6_322$. It was revealed that the *x* value is limited to 0.33 at maximum to maintain the hexagonal phase for these three compounds [1,4,7]. These three M*x*WO_3 compounds show interesting electrical properties, such as superconductivity at very low temperatures for $0.15 < x < 0.33$. The superconducting transition temperature T_c ranges between 1 and 7 K and increases gradually towards lower *x* values [3]. Furthermore, the hexagonal M*x*WO_3 phase is also regarded as being highly attractive in solar filter applications, because the absorption is small enough in the visible range but is strong in near infrared (NIR) lights [8]. The NIR absorption increases with increasing *x* value of M*x*WO_3 has been reported in the literatures [1,9,10].

The alkali-HTB phase was first reported by Magneli and Blomberg in 1951 [11]. Later, Magneli found that the unit cell dimensions of the tungsten bronzes were approximately the same irrespectively of the alkali metal atoms being potassium, rubidium or cesium [12]. He carried out the first single-crystal X-ray diffraction study on a tiny $Rb_{0.27}WO_3$ crystal and indicated that the crystal structure was determined to possess a hexagonal symmetry with a space group of $P6_3/mcm$ [9]. However, there have been several crystal-structure determinations of three compounds since the original model proposed by Magneli. The space group of either $P6_3/mcm$ or $P6_322$ has been reported in few cases [13–17].

In order to solve the structural discrepancy as described above, we need to prepare alkali-HTB samples. The traditional methods for preparing the hexagonal tungsten bronze by the reactions of various oxide materials at higher temperatures in reducing atmospheres have been reported [1,7,18]. These preparations mostly give polycrystalline material or the quality of crystals not good enough to study their structural characteristics. Compared with powder diffraction data, more accurate structural details can be

* Corresponding author.
E-mail address: jslee@mail.nptu.edu.tw (J.-S. Lee).

http://dx.doi.org/10.1016/j.jcrysgro.2017.02.044
0022-0248/© 2017 Elsevier B.V. All rights reserved.

obtained by single crystal X-ray diffraction (SCXRD) data. Therefore, two crystal synthesis techniques, fused salt electrolysis as well as chemical transport method, have already been reported in the literatures. The crystal growth of tungsten bronzes by fused salt electrolysis was first reported by Scheiblert in 1860 [19]. As far as we know, only non-hexagonal NaxWO$_3$ and tetragonal KxWO$_3$ crystals have been grown by fused salt electrolysis with predictable compositions [19,20]. Intergrown clusters of different crystalline phases often occurred without using a seed crystal. Growing crystals of alkali metal hexagonal tungsten bronzes (HTB) and tetragonal tungsten bronzes (TTB) have also been made by chemical transport in a temperature gradient. However, extremely toxic materials, such as $HgCl_2$, $HgBr_2$, HgI_2, and Cl_2, were employed as transport agents in the synthesis route [21,22]. In order to synthesize the alkai-HTB crystals with quality good enough for SCXRD, we have developed a new safe and easy route via molten-salt method in the present study.

The crystal structures of isostructural $Cs_{0.33}WO_3$, $Rb_{0.33}WO_3$ and $K_{0.30}WO_3$ were determined using as-grown crystals in the study. One of the main structural features in the hexagonal $Cs_{0.33}WO_3$, $Rb_{0.33}WO_3$ and $K_{0.30}WO_3$ is the existence of the six-membered WO_6 octahedral rings running parallel to the c axis, as shown in Fig. 1. The top and bottom vertices of the octahedral pyramids in each WO_6 octahedron are O1 oxygen atoms. Others are four oxygen atoms (O2), coplanar with one W atom in each WO_6 octahedron. The rings interconnected by sharing one of WO_6 octahedra exhibit a layered, planar structure parallel to (0001). Within the ring, two of O2 atoms in each WO_6 group are shared by adjacent WO_6 groups on either side. Each layer is linked by O1 atoms to form a three-dimensional framework. The alkali element (M) such as Cs, Rb and K are accommodated in the broad channels and lie midway between two six-membered WO_6 octahedra rings. Each M atom is coordinated with 12 oxygen atoms (O2) forming a hexagonal prism. Since the M^+ cations have different effective radii, systematic variation in the geometry of the WO_6 and MO_{12} groups is expected. One of the purposes of this study is to examine the structural trends as well as the influence of alkali metals on the stability for alkali-HTB compounds. Using SCXRD analysis, this study shows that the geometry of the WO_6 groups varies in a systematic and expected manner.

2. Experimental procedures

The polycrystalline samples of CsxWO$_3$, RbxWO$_3$ and KxWO$_3$ were first synthesized using a high-temperature solid-state reaction technique with high-purity (AR grade) ingredients: Cs_2CO_3, Rb_2CO_3, K_2CO_3 and H_2WO_4 (Sigma-Aldrich Co.). These reactants with appropriate molar ratio in wet (de-ionized water) medium were heated and mixed by a magnetic stirrer with a hotplate for several hours. The mixed material was calcined at an optimized temperature at 700 °C for 5 h in alumina crucible in a reducing atmosphere in the presence of carbon black. All the resulting powders of tungsten bronzes exhibit a deep blue color. The phase compositions of these samples were determined by X-ray diffraction analysis (XRD, Shimadzu XRD-6000) using the CuKα radiation (λ = 1.5418 Å). The absorption properties of these three samples were investigated by using a Jasco V670 UV–Vis-NIR spectrophotometer. In order to produce single crystals via molten-salt method, these synthetic tungsten bronze powders were then combined with the salt fluxes of CsCl/NaCl, RbCl/NaCl and KCl/NaCl, respectively. These mixtures were ground and then dried at 120 °C for 1 day. These initial substances were sealed into evacuated silica ampoules and annealed at higher temperatures. The growth process was finished by cooling the ampoules in air. Synthesized tungsten bronze crystals were released from flux by washing with deionizated water. Elemental analysis was performed on the synthetic crystals with an energy dispersive X-ray spectrometer (EDX, Oxford INCA 350X-act) attached to a JEOL JSM-6390 scanning electron microscope. EDX and structural refinement of SCXRD data revealed the average chemical composition of as-grown crystals. Crystals of each product were mounted on glass fibers for diffraction. The as-grown crystals of these three compounds was selected for SCXRD intensity data collection at room temperature using a Bruker AXS SMART CCD diffractometer equipped with Mo radiation (λ = 0.71073 Å). Processing of the data was accomplished with the use of the program SAINT; an absorption correction was applied to the data using the SADABS program [23]. The unit cell dimensions were determined by a least-squares fit of collected reflections. The crystal structure was analyzed and refined with a full-matrix least-squares method of the Bruker SHELTAL Version 5.1 software package. The crystallographic data of our three as-grown crystals are summarized in Table 1. Table 2 also presents their atom coordinates and isotropic displacement coefficients. Raman measurements were performed by using a microscopic Raman system (RAMaker, Protrustech Co., Ltd., Taiwan). An exciting line of 532 nm was supplied by a diode laser (CNI) with a power of 12 mW. The exposure time was 10 s with 10 accumulations. Calibration was done using a silicon standard where the band is generally observed at 520 cm^{-1}. The corresponding spectral resolution was in the range of 1 cm^{-1}.

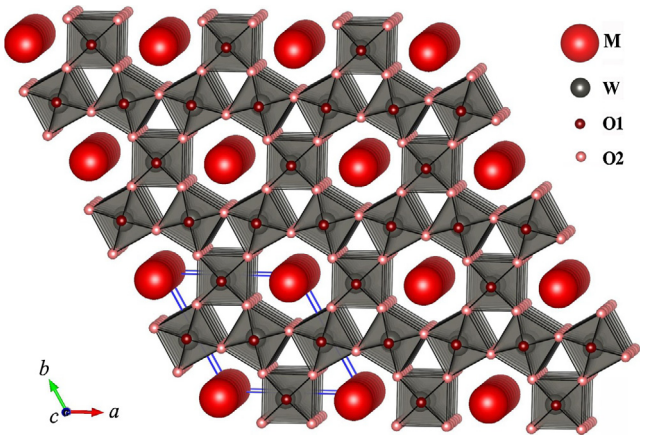

Fig. 1. Crystal structure of $Cs_{0.33}WO_3$ framework projected on a–b planes.

3. Results and discussion

3.1. Sample preparations

Fig. 2 exhibits the typical XRD patterns of the synthesized CsxWO$_3$, RbxWO$_3$ and KxWO$_3$ powders annealed at 700 °C for

Table 1
Unit cell constants and data-collection parameters of three flux-grown HTB specimens.

Chemical formula	$Cs_{0.33}WO_3$	$Rb_{0.33}WO_3$	$K_{0.30}WO_3$
Space group	$P6_3/mcm$	$P6_3/mcm$	$P6_3/mcm$
a (Å)	7.4035(2)	7.3842(3)	7.3742(5)
c (Å)	7.6144(2)	7.5682(3)	7.5169(5)
Cell volume (Å^3)	361.4(1)	357.4(1)	354.0(1)
Density (calc.)	7.612	7.258	6.859
Absorption coeff. (mm^{-1})	52.607	54.951	49.180
Reflections collected	4743	3954	4099
R_1 (%) ($I > 2\sigma(I)$)	1.70	1.70	3.01
R_1 (%) (all data)	1.98	1.70	3.01
Largest Δe/Å^3	2.10/−2.98	1.22/−1.96	2.91/−2.97

Table 2
Atomic coordinates and their isotropic displacement parameters of three flux-grown HTB specimens.

Atoms		$Cs_{0.33}WO_3$	$Rb_{0.33}WO_3$	$K_{0.30}WO_3$
M#	*x*	0	0	0
	y	0	0	0
	z	0	0	0
	U_{eq} [a]	0.017(1)	0.004(1)	0.114(13)
W	*x*	4855(1)	0.4830(1)	4796(1)
	y	0	0	0
	z	0.2500	0.2500	0.2500
	U_{eq}	0.003(1)	0.003(1)	0.008(1)
O1	*x*	0.5000	0.5000	0.5000
	y	0	0	0
	z	0	0	0
	U_{eq}	0.007(3)	0.0014(3)	0.023(4)
O2	*x*	4199(13)	4213(12)	4199(13)
	y	2120(12)	2071(11)	2120(12)
	z	0.2500	0.2500	0.2500
	U_{eq}	0.009(1)	0.0012(1)	0.021(2)

[a] Equivalent isotropic U defined as one third of the trace of the orthogonalized U_{ij} tensor; #M = Cs/Rb/K.

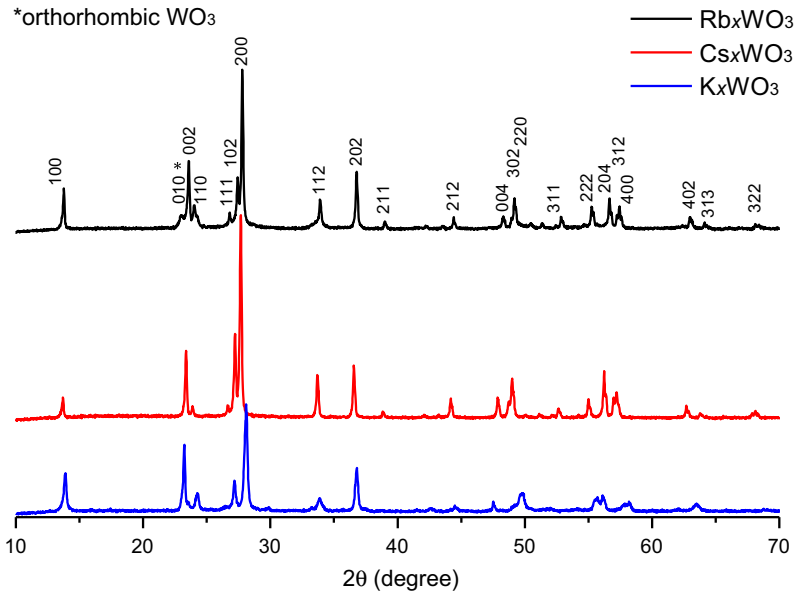

Fig. 2. XRD patterns of synthesized Cs*x*WO_3, Rb*x*WO_3 and K*x*WO_3 powders annealed at 700 °C for 5 h.

5 h. All diffraction peaks of Cs*x*WO_3 and K*x*WO_3 powders could be indexed to the crystalline Cs-HTB (JCPDS No. 83-1334) and K-HTB (JCPDS No. 49-0541) phases, respectively. The XRD peaks of our synthetic Rb*x*WO_3 powder almost conform to those reported in the JCPDS data (JCPDS No. 75-0440). However, a minor orthorhombic WO_3 phase was also detected. The presence of the WO_3 phase may be due to incomplete chemical reaction between reactant materials. The absorption spectra of three samples clearly exhibit the absorption properties illustrated in Fig. 3. The maximum visible light transmission for three samples occurred at wavelengths of about 550 nm. The NIR rays were significantly cut off in the range of 900–1600 nm for Cs*x*WO_3 sample. This result suggests that the NIR absorption of Cs*x*WO_3 is evidently superior to Rb*x*WO_3 and K*x*WO_3 as these powders are formed by annealing at 700 °C.

Reactions of early transition metal oxides with metals in CsCl/NaCl are being explored to synthesize reduced metal oxide phases. This is also a useful alternative for syntheses of tungsten bronze phases in the study. Mixtures of CsCl and NaCl in 13:7 M ratio produce a eutectic which melts at 495 °C [24]. The eutectic temperature is lower than those of CsCl (645 °C) or NaCl (801 °C). So the molten salt with temperature lower than 800 °C would be obtained easily. When the molten salt solidifies as it is cooled down in crucible, the separation of salt mixture (CsCl and NaCl) and crucible is much easier than that of simple salt (NaCl) and crucible. The sealed silica ampoules were heated in a muffle furnace to 700 °C in 2.5 h, slowly cooled down to 650 °C in 2 h, held at this temperature for 48 h, and cooled down to 600 °C in 48 h. Finally, the products were taken off from the furnace as cooled down to room temperature. After these procedures, the reactant materials Cs_xWO_3 dissolved in molten CsCl/NaCl flux successfully yield black crystals of $Cs_{0.33}WO_3$. Crystals up to 6 mm in lengths can be obtained in the crystal growth route, as shown in Fig. 4. These as-grown crystals mostly occur as hexagonally prismatic crystals with or without capped by the hexagonal bipyramid. The chemical formula of synthetic cesium tungsten bronze crystal is determined to be $Cs_{0.33}WO_3$. According to our experimental data, the crystal size seems to be

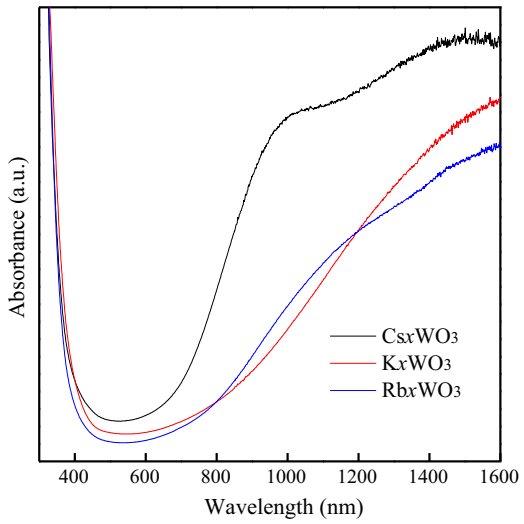

Fig. 3. Absorption spectra of three synthetic powders annealing at 700 °C.

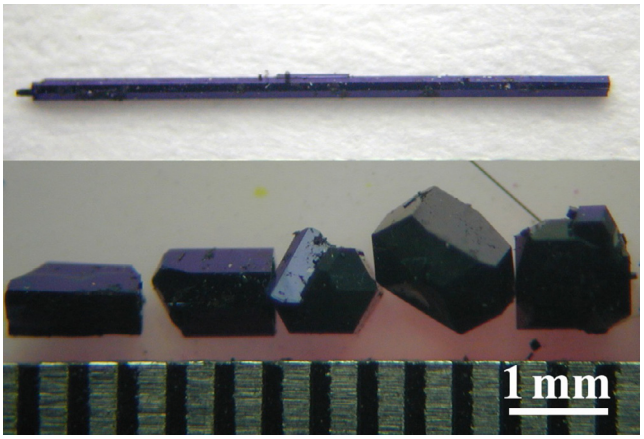

Fig. 4. Photographs of as-grown $Cs_{0.33}WO_3$ crystals.

dependent on the crystallization temperature and the ratio of Cs_x-WO_3/flux (Table 3). As a result, it may be helpful to produce bigger crystals in the molten salt method with a higher ratio of Cs_xWO_3/flux reactants heated at higher temperatures.

In the cases of growing K-HTB crystals, KCl/NaCl salt fluxes were used in the work. The lowest liquidus temperature (650 °C) of the KCl/NaCl salt mixtures is at 0.5 KCl-0.5 NaCl [25]. Hence, an equimolar KCl and NaCl mixture is used as the flux to grow potassium tungsten bronze crystals. The mixtures of K*x*WO_3 and fluxes in sealed tubes were heated to 800 °C in 3 h, slowly cooled down to 750 °C in 2 h, kept at750 °C for 48 h, cooled down to 700 °C in 48 h, and finally cooled the tubes in air. The synthetic K*x*WO_3 powder in this KCl/NaCl flux also resulted in the formation of black crystals with crystal size up to 1 mm. Based on the EDX analysis, these synthetic crystals are found to be of the potassium tungsten bronze $K_{0.30}WO_3$. Their crystal forms are very similar to those of as-grown Cs-HTB. On the other hand, the RbCl/NaCl fluxes were used to grow rubidium tungsten bronze crystals. The 14:11 M ratio of RbCl and NaCl forms a eutectic which melts at 550 °C [25] and the mixture was used as the flux medium. The crystal growth processes of rubidium tungsten bronze are very similar to those of Cs-HTB. The compound $Rb_{0.33}WO_3$ was formed in the preparation route with smaller crystal size of 0.2 mm in length. In comparison with Cs- and K-HTBs, it seems that to prepare big Rb-HTB crystals via molten salt method is not easier. It is speculated that this result is due to the existence of a minor WO_3 phase in reactants. Further study may be needed to verify validity of this argument.

To preliminarily examine crystalline phases of synthetic products, the Raman spectra obtained from these three as-grown crystals are shown in Fig. 5. These observed spectra have good agreement with the reported spectra of three different alkali-HTB compounds [26]. The common feature for each sample is the presence of the 850 cm^{-1}–1050 cm^{-1} bands, which is assigned to the stretching vibrations of the terminal W=O bonds [27]. The strong and broad Raman peaks in the region of 850 cm^{-1}–500 cm^{-1} were observed due to the asymmetric stretching modes of O—W—O bonds [28]. Maczka at al. indicated that when tungsten ion is replaced by larger ions, much greater squeezing of WO_6 polyhedra can be revealed from the variations of Raman peak positions in this region and thus the distances of W—O2 within the *xy* mirror plane are more shortening correspondingly [27]. They suggested that larger Rb^+ or Cs^+ ionic substitution for K^+ ion is also responsible for the small increment in Raman frequency in this region. The interatomic distances of W—O and M—O as well as those angles in O1—W—O2 for these alkali-HTB crystals are listed in Table 4. The results from the crystallographic data reveal that the <W—O2> bond distances gradually increase with a slight decrease in Raman bands from K^+ to Cs^+ ions (Fig. 4 and Table 4). As a result, the reported squeezing effect of WO_6 octahedra is not observed in the work when K^+ ions are replaced by larger Rb^+ or Cs^+ ions.

3.2. Structural trends

As described above, the three isostructural compounds have WO_6 octahedra with one W atom and four O2 oxygen atoms situated on a mirror plane parallel to *xy* plane. In fact, all of WO_6 in HTB are of irregular octahedra with the W atoms located off the

Table 3
Crystal growth of three HTB crystals using different amounts of reactants at specific temperatures.

Exp. no.	Nominal compositions of crystals	Amounts of M*x*WO_3 powder (M = Cs, Rb, K)	Amounts of MCl/NaCl fluxes (M = Cs, Rb, K)	Maximum heating temperature	Average crystal size
1	Cs*x*WO_3	1 g	1.205 g/0.225 g	650 °C	Polycrystalline
2	$Cs_{0.30}WO_3$	0.01 g	1.205 g/0.225 g	650 °C	0.2 mm
3	$Cs_{0.33}WO_3$	0.05 g	1.205 g/0.225 g	650 °C	0.2 mm
4	$Cs_{0.33}WO_3$	0.01 g	6.035 g/1.125 g	700 °C	1 mm
5	$Cs_{0.33}WO_3$	0.05 g	6.035 g/1.125 g	700 °C	2 mm
6	$Cs_{0.33}WO_3$	1 g	6.035 g/1.125 g	700 °C	0.5 mm
7	$Cs_{0.33}WO_3$	0.05 g	12.05 g/2.225 g	700 °C	2 mm
8	$Rb_{0.33}WO_3$	0.05 g	0.677 g/0.257 g	700 °C	0.2 mm
9	Rb*x*WO_3	0.01 g	3.385 g/1.285 g	750 °C	Polycrystalline
10	Rb*x*WO_3	0.05 g	3.385 g/1.285 g	750 °C	Polycrystalline
11	$K_{0.30}WO_3$	0.01 g	3.73 g/2.92 g	800 °C	0.2 mm
12	$K_{0.30}WO_3$	0.05 g	3.73 g/2.92 g	800 °C	0.5 mm

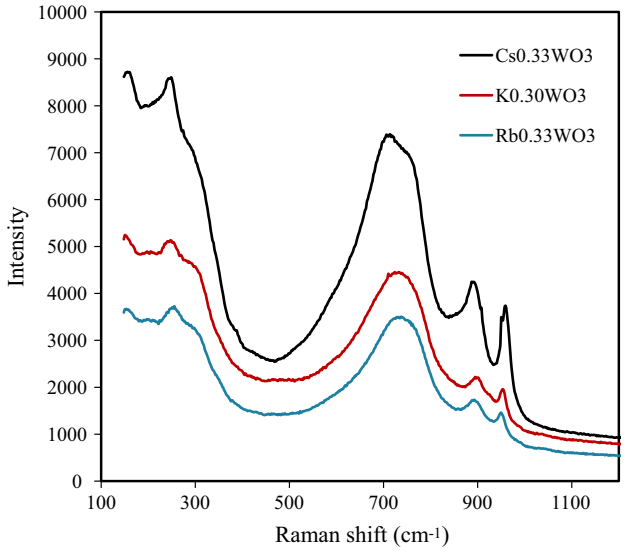

Fig. 5. Raman spectra of three as-grown compounds.

Table 4
Bond distances and selected bond angles of three flux-grown HTB specimens.

	$Cs_{0.33}WO_3$	$Rb_{0.33}WO_3$	$K_{0.30}WO_3$
Distances (Å)			
W—O1 (x2)	1.907(1)	1.896(1)	1.885(1)
W—O2 (x2)	1.860(8)	1.852(7)	1.839(9)
W—O2 (x2)	1.985(8)	1.980(8)	1.990(9)
<W—O2>	1.922	1.916	1.914
<W—O>	1.917	1.909	1.904
V_{oct} (Å^3):	2.285	1.967	1.812
Angles (°)			
O1—W—O1	173.53(4)	172.42(3)	170.89(4)
O1—W—O2	92.21(2)	92.55(2)	93.04(2)
O1—W—O2	87.61(2)	87.18(2)	86.58(2)
<O1—W—O2>	89.91	89.86	89.81
λ_{oct}:	1.0030	1.0039	1.0074
σ^2_{oct} (deg^2)	3.5214	3.1470	2.2492
Distances (Å)			
M—O2	3.297(7)	3.292(6)	3.282(8)
O2—O2[a]	3.807	3.784	3.759
W—W[a]	3.813	3.792	3.770

M: Cs/Rb/K; V_{oct}: volume of WO_6 octahedron; λ_{oct}: mean quadratic elongation of WO_6; σ^2_{oct}: bond angle variance of WO_6.
[a] Atomic distances between layers; < >: average value of bond lengths or bond angles.

center of the polyhedra. The M^+ (= Cs, Rb, or K) cation is coordinated to twelve O2 atoms, in which each M—O2 bond distances is identical. According to our SCXRD data, unit-cell parameters of *a*, *c* and *V* (the cell volume) are plotted against the ionic radii (r_M) of the 12-coordinated M^+ cations with ionic radii according to Shannon [29]. The unit-cell parameters for the isostructural HTBs are in good agreement with those obtained previously [3,10,11,13,14,23,27], as shown in Figs. 6 and 7. The increase in cell parameters *a* and *c* is in proportion to the r_M (Fig. 6). The *V* increases linearly with increasing the ionic radii of M^+ cation (Fig. 7). The M—O2 bond lengths also increase from $K_{0.30}WO_3$ to $Cs_{0.33}WO_3$ (Table 4). The interesting geometrical features of the WO_6 group are also plotted against ionic radii, r_M (Figs. 8 and 9). The volume of WO_6 octahedron linearly increases with increasing the size of r_M. The average <W—O> distance lengthens from the increase in size of the M^+ cation in a near-linear manner. To measure the distortion degree of WO_6, two distortion parameters for coordination polyhedra introduced by Robinson et al. [30] are

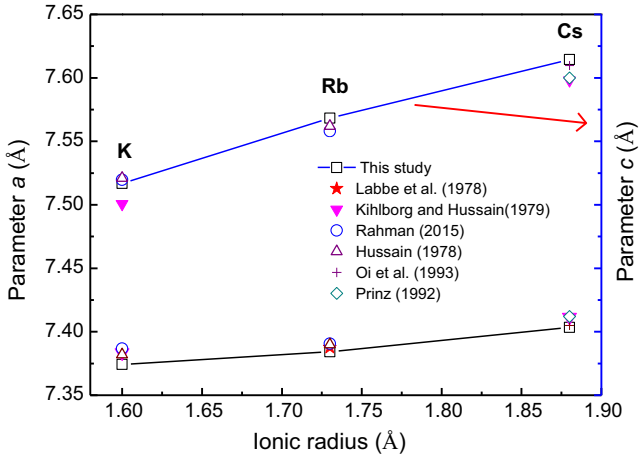

Fig. 6. Dependence of the *a*, *c* unit-cell parameters on the ionic radius, r_M, of the twelve-coordinated M^{2+} cation.

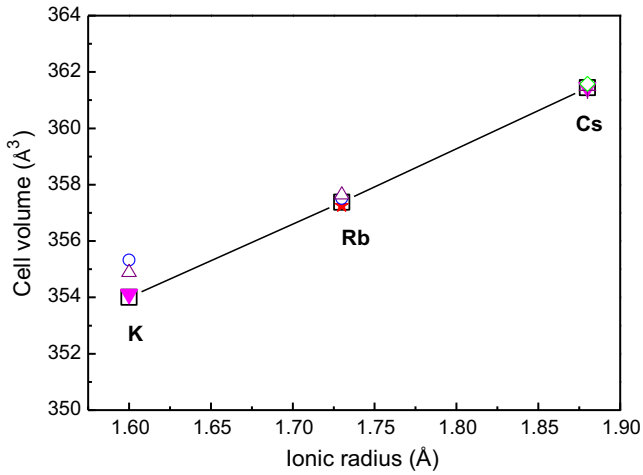

Fig. 7. Variation of the unit cell volumes as a function of the ionic radius, r_M, of the twelve-coordinated M^{2+} cation.

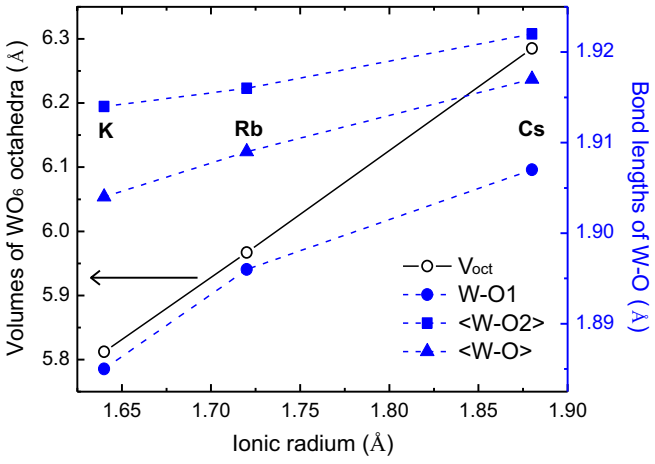

Fig. 8. Volumes of WO_6 octahedron and bond lengths of W—O versus the ionic radius r_M, of the twelve-coordinated M^{2+} cation.

employed in the work. Regular polyhedra have a quadratic elongation (λ) of one and a bond angle variance (σ) of zero. These two parameters will increase with the distortion of polyhedra. The data

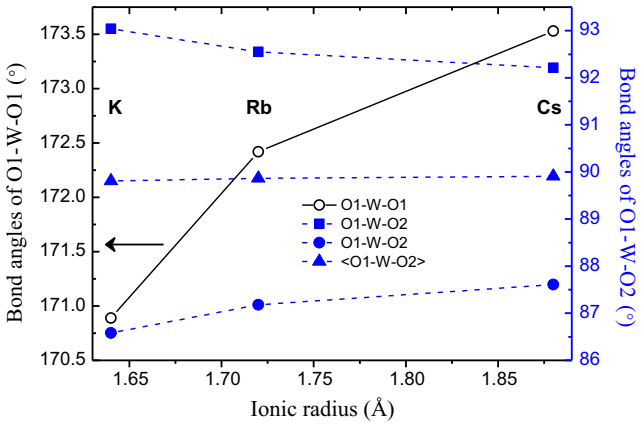

Fig. 9. Bond angles of O1—W—O1 and O1—W—O2 versus the ionic radius r_M, of the twelve-coordinated M^{2+} cation.

from this study shows that the WO_6 polyhedron becomes less distorted with increment in size of the M^+ cation (Table 4). Two kinds of the O1—W—O2 angles in WO_6 octahedra gradually approach the right angle from $K_{0.30}WO_3$ to $Cs_{0.33}WO_3$ (Fig. 9). Therefore, the geometry of the WO_6 group becomes more regular from $K_{0.30}WO_3$ to $Cs_{0.33}WO_3$ owing to the fact that individual W—O distances and O1—W—O2 angle are closer to the average values (Figs. 8 and 9). In addition, the O1—W—O1 angle is progressively close to 180° due to the increasing r_M. That is, W atom is closer to center of the WO_6 octahedra with increasing the ionic radii of M^+ cation. Consequently, the $K_{0.30}WO_3$ structure is most distorted and the $Cs_{0.33}WO_3$ structure is least distorted in terms of the geometry of the WO_6 polyhedra. A previous report [10] indicated that the incorporation of Cs^+ into the hexagonal tunnels will induce the structure distortion of WO_6 octahedral framework owing to the bigger size of Cs^+ ion (1.88 Å). On the contrary, the incorporation of the smaller K^+ ion (1.64 Å) results in more distorted WO_6 octahedra according to the structural details revealed in the study. Similar conclusion has been drawn by Maczka et al. on the basis of variations in Raman spectra of these three compounds [27]. They suggested that there is a smaller distortion (stronger stability) of the Cs-HTB compared with the K- and Rb-HTBs.

The crystal structure of hexagonal M*x*WO_3 phases generally contain tungsten atoms in mixed chemical valence (W^{6+} and W^{5+}). Considering the Coulomb's law, the repulsive force between two adjacent high-valence tungsten ions will be significantly enhanced due to the shortening of their distance. In order to minimize the effect of the repulsive force, it is not easy to make two WO_6 octahedra between layers to close each other. Consequently, the W-W and O2—O2 distances between layers as well as W—O1 shorten only a little after the incorporations of smaller alkali ions into the lattice site (Table 4). Although the extent of change in shortening is small, it may be responsible for the larger WO_6 distortion induced by Coulomb repulsive force in $K_{0.30}WO_3$. While the size of ionic radius r_M increases from $K_{0.30}WO_3$ to $Cs_{0.33}WO_3$, the variations in distances between layers is small. Thereby, the largest Cs^+ ion would be quite comfortable in the channel whereas the relatively small K^+ ion would have more space to wonder around. This may be attributed to the near equal length between the radius of Cs^+ ion and the available radius of the site in the hexagonal tunnel. This may also explain the remarkable increase in the isotropic displacement parameters U_{eq} from $Cs_{0.33}WO_3$ to $K_{0.30}WO_3$, as listed in Table 2.

Based on our experimental data, K—O2 and Rb—O2 bond distances in the HTB seem to be too long in comparison with normal ones [31]. Brown and Shannon [32] suggested that the strength of the bond (*s*) between a cation and its neighboring oxygen ion correlates very well with the bond distance of separation *R*. The relationship is of the form $s = (R/R_0)^{-N}$ where R_0 and *N* are empirically determined parameters. On the basis of our M—O distances and the previously reported parameters [33], the bond strengths (*s*) are determined to be 0.093, 0.062 and 0.045 for the hexagonal $Cs_{0.33}WO_3$, $Rb_{0.33}WO_3$ and $K_{0.30}WO_3$, respectively. These results reveal that the bond strength of M—O2 is coherently weakened with the decrease in radii (r_M) of M^+ cation. Interestingly, the sodium tungsten bronze of $P6_3$/mcm structure has not been discovered so far. If a relative small Na^+ (1.39 Å) might incorporated into the hexagonal channel, it would make the Coulomb repulsive force more strong and thus WO_6 octahedron more distorted based on the structural trend as described above. In addition, the relatively small Na^+ ion would rattle around more obviously in the ring channel. Particularly, Na-HTB ($P6_3$/mcm) crystals have not been formed in the molten salt syntheses containing NaCl flux. A previous report in the literature [7] showed that pure hexagonal phases cannot be prepared by adding cesium and sodium to the crystal structures in tungsten trioxides. Consequently, the study implies that there would be a higher degree of structural instability for Na-HTB $P6_3$/mcm phase.

This study shows that several well-defined structural trends occur in the isostructural HTB ($P6_3$/mcm) compounds; in particular, the geometry of the WO_6 octahedra changes in a regular manner. These structural trends arise from the effective size of the M^+ cation (r_M: K < Rb < Cs) that is coordinated to twelve O2 atoms. Similar results were also obtained for the framework silicates, where the geometry for SiO_4 group changes in a regular manner [34]. Furthermore, the geometry of the CO_3 group for the orthorhombic carbonates also changes in a regular way with ionic radius of M^{2+} cation [35].

4. Conclusions

Three compounds, $Cs_{0.33}WO_3$, $Rb_{0.33}WO_3$, and $K_{0.30}WO_3$, have been grown from the reactant materials C*sx*WO_3, R*bx*WO_3 and K*x*WO_3 dissolved in molten CsCl/NaCl, RbCl/NaCl and CsCl/NaCl fluxes, respectively. This study shows that the crystal structures of the three tungsten bronze compounds are essentially similar with a space group of $P6_3$/mcm. Several well-defined structural trends can be found in the three isostructural HTB compounds. The cell parameters increase with increasing radii of the M^+ cations (r_M) that is coordinated to twelve O atoms. In particular, the distortion of WO_6 octahedra increases from $Cs_{0.33}WO_3$ to $K_{0.30}WO_3$. The geometry of the WO_6 octahedron is more regular with increasing r_M. To minimize the effect of the repulsive force of adjacent high-valence W^{5+}/W^{6+} ions, it leads to the remarkable increase in the isotropic displacement parameters from $Cs_{0.33}WO_3$ to $K_{0.30}WO_3$. According to the parameters and bond strength of M—O, the structural instability will increase with the decreasing r_M. The study shows that these structural trends arise from the effective size of the M^+ cation.

Acknowledgements

The authors are grateful to Miss P.L. Cheng who collected the X-ray intensity data. We also thank Associate Professor H.J. Yang of the Department of Earth Science in National Cheng Kung University for his help in the ICP-MS analysis. Thanks are also extended to Professor I. C. Leu of the Department of Materials Science in National University of Tainan for providing assistance in the UV/Vis/NIR operation. This work was supported by grant MOST103-2116-M105-001 from the Ministry of Science and Technology, R. O.C.

Appendix A. Supplementary material

Supplementary data associated with this article can be found, in the online version, at http://dx.doi.org/10.1016/j.jcrysgro.2017.02.044.

References

[1] H. Takeda, K. Adachi, Near infrared absorption of tungsten oxide nanoparticle dispersions, J. Am. Ceram. Soc. 90 (12) (2007) 4059–4061.
[2] J. Liu, J. Luo, F. Shi, S. Liu, C. Fan, Q. Xu, G. Shao, Synthesis and characterization of F-doped $Cs_{0.33}WO_{3-x}F_x$ particles with improved near infrared shielding ability, J. Solid State Chem. 221 (2015) 255–262.
[3] A. Hussain, R. Gruehn, C.H. Ruscher, Crystal growth of alkali metal tungsten bronzes M*x*WO_3 (M = K, Rb, Cs) and their optical properties, J. Alloys Compd. 246 (1997) 51–61.
[4] A. Hussain, Phase analyses of potassium, rubidium and cesium tungsten bronzes, Acta Chemica Scandinovica A32 (1978) 479–484.
[5] A.E. El-Sayed, S.M.A. Mousa, Some properties of sodium tungsten bronzes as a function of sodium concentration, Indian J. Chem. Technol. 12 (2005), 403-308.
[6] T. Guo, B.P. Jelle, Visible-light-driven photochromism of hexagonal sodium tungsten bronze nanorods, J. Phys. Chem. C117 (26) (2013) 13753–13761.
[7] K. Moon, J.J. Cho, Y.B. Lee, P.J. Yoo, C.W. Bark, J. Park, Near infrared shielding properties of quaternary tungsten bronze nanoparticle $Na_{0.11}Cs_{0.22}WO_3$, Bull. Korean Chem. Soc. 34 (2013) 731–734.
[8] F. Shi, J. Liu, X. Dong, Q. Xu, J. Luo, H. Ma, Hydrothermal synthesis of Cs*x*WO_3 and the effects of N_2 annealing on its microstructure and heat shielding properties, J. Mater. Sci. Technol. 30 (2014) 342–346.
[9] C. Guo, S. Yin, L. Huang, T. Sato, Synthesis of one-dimensional potassium tungsten bronze with excellent near-infrared absorption property, ACS Appl. Mater. Inter. 3 (7) (2011) 2794–2799.
[10] C. Guo, S. Yin, M. Yan, T. Sato, Facile synthesis of homogeneous Cs*x*WO_3 nanorods with excellent low-emissivity and NIR shielding property by a water controlled-release process, J. Mater. Chem. 21 (2011) 5099–5105.
[11] A. Magneli, B. Blomberg, Contribution to the knowledge of alkali tungsten bronzes, Acta Chemica Scandinovica 5 (1951) 372–378.
[12] A. Magneli, Studies on the hexagonal tungsten bronzes of potassium, rubidium and cesium, Acta Chemica Scandinovica 7 (1953) 315–324.
[13] A.P. Labbe, M. Goreaud, B. Raveau, J.C. Monier, Etude comparative des structures M*x*WO_3 de type bronze hexagonal. I. Analyse structurale des bronzes de composition $M_{0.30}WO_3$ stereochimie des elements M = Rb^+, Tl^+ et In^+, Acta Crystallogr. A B34 (1978) 1433–1438.
[14] L. Kihlborg, A. Hussain, Alkali metal location and tungsten off-center displacement in hexagonal potassium and cesium tungsten bronzes, Mater. Res. Bull. 14 (1979) 667–674.
[15] M.F. Pye, P.G. Dickens, A structure sturdy of hexagonal potassium tungsten bronze, $K_{0.26}WO_3$, Mater. Res. Bull. 14 (1979) 1397–1402.
[16] J. Oi, A. Kishimoto, T. Kudo, Hexagonal and pyrochlore-type cesium tungstate synthesized from cesium peroxo-polytungstate and their redox chemistry, J. Solid State Chem. 103 (1993) 176–185.
[17] H. Prinz, U. Muller, M.L. Ha-Eierdanz, Ein neues Syntheseverfahren fur die Wolframbronze $Cs_{0.29}WO_3$ und ihre Kristallstruktur, Zeitschrift für anorganische und allgemeine Chemie 609 (1992) 95–98.
[18] J.Y. Kim, H.J. Yoon, S.Y., Jeong, S, Lee, G.J. Shin, K.H. Choi, Effect of CsxWO3 nanoparticles content and atomic ratio for near infrared cut-off characteristics, in: 2012 3rd International Conference on Biology, Environment and Chemistry, vol. 46, 9.
[19] H.R. Shanks, Growth of tungsten bronze crystals by fused salt electrolysis, J. Cryst. Growth 13 (14) (1972) 433–437.
[20] E. Banks, E.W. Fleischmann, L. Meites, On the nature of the species reduced during the electrochemical synthesis of tungsten bronzes, J. Solid State Chem. 1 (3/4) (1970) 372–375.
[21] A. Hussain, R. Gruehn, Crystal growth of hexagonal potassium tungsten bronze by chemical transport, J. Cryst. Growth 108 (1991) 831–833.
[22] A. Hussain, R. Gruehn, C.H. Ruscher, Crystal growth of alkali metal tungsten bronzes M*x*WO_3 (M = K, Rb, Cs) and their optical properties, J. Alloy. Compd. 246 (1997) 51–61.
[23] G.M. Sheldrick, SADABS, Programs for Scaling and Correction of Area Detection Data, University of Göttingen, Göttingen (Germany), 1996.
[24] P. Mahjoor, S.E. Latturner, Salt-flux synthesis of complex oxides: $Cs_{0.33}MoO_3$, $CsFe(MoO_4)_2$, and the inverse salt-inclusion phase $Cs_2Mo_{0.65}O_{0.21}Cl_{5.44}$, Phil. Mag. 92 (19–21) (2012) 2582–2595.
[25] J. Sangster, A.D. Pelton, Phase diagrams and thermodynamic properties of 70 binary alkali halide systems having common ions, J. Phys. Chem. Ref. Data 16 (3) (1987).
[26] M. S. Rahman, Synthesis, Characterization and Structure-Property Relationship of Alkali Metal Tungsten Bronzes, Dissertation of University of Bremen, German, 2015.
[27] M. Maczka, J. Hanuza, A. Majchrowski, Vibrational properties of ferroelectric hexagonal tungsten bronzes AB*x*W3−*x*O_9, where A = K, Rb, Cs and B =Nb, Ta, Zr, Cr, J. Raman Spectrosc. 32 (2001) 929–936.
[28] M. Boulova, N. Rosman, P. Bouvier, G. Lucazeau, High-pressure Raman study of microcrystalline WO_3 tungsten oxide, J. Phys. Con. Matter 14 (2002) 5849–5863.
[29] R.D. Shannon, Revised effective ionic radii and systematic studies of Interatomic distances in halides and chalcogenides, Acta Crystallogr. A A32 (1976) 751–767.
[30] K. Robinson, G.V. Gibbs, P.H. Ribb, Quadratic elongation: a quantitative measure of distortion in coordination polyhedral, Science 172 (1971) 567–570.
[31] C.H. MacGillavry, G.D. Rieck (Eds.), International Tables for X-ray Crystallography vol. 3: Physical and Chemical Tables, 2nd ed., Kynoch, Birmingham, U.K., 1985, pp. 258–259.
[32] I.D. Brown, R.D. Shannon, Empirical bond-strength-bond-length curves for oxides, Acta Crystallogr. A A29 (1973) 266–282.
[33] I.D. Brown, D. Altermatt, Bond-valence parameters obtained from a systematic analysis of the inorganic crystal structure database, Acta Crystallogr. A B41 (1985) 244–247.
[34] S.M. Antao, I. Hassan, J. Wang, P.L. Lee, B.H. Toby, State-of-the-art high-resolution powder X-ray diffraction (HRPXRD) illustrated with Rietveld structure refinement of quartz, sodalite, tremolite, and meionite, Can. Mineral. 46 (2008) 1501–1509.
[35] S.M. Antao, I. Hassan, The orthorhombic structure of $CaCO_3$, $SrCO_3$, $PbCO_3$, and $BaCO_3$: linear structural trends, Can. Mineral. 47 (2009) 1245–1255.